Use of image correlation system to study the bond behavior of FRCM-concrete joints

C. Sabau[1], J.H. Gonzalez-Libreros[2], L.H. Sneed[3], G. Sas[4], C. Pellegrino[2], B. Täljsten[1]

[1] *Department of Civil, Environmental and Natural Resources Engineering, Luleå University of Technology, 971 87 Luleå, Sweden*

[2] *Department of Civil, Environmental and Architectural Engineering, University of Padua, Via Marzolo 9, 35131 Padova, Italy*

[3] *Department of Civil, Architectural and Environmental Engineering, Missouri University of Science and Technology, Rolla, MO 65409, USA*

[4] *Department of Infrastructure, Materials and Structural Engineering, NORUT, Rombaksveien E6-47, N-8504 Narvik, Norway*

Corresponding author: L.H. Sneed[3], e-mail: sneedlh@mst.edu, telephone number: +1 573-341-4553, fax number: +1 573-341-4729

Abstract

This paper presents a non-contact measurement approach, based on digital photogrammetry, applied to the experimental study of the bond behavior of fiber reinforced cementitious matrix composite (FRCM) - concrete joints tested in single-lap direct shear tests. The use of digital photogrammetry techniques and traditional contact measurement approaches for determining displacement and strain are investigated and compared. The results show that measurements of strain in the fiber bundles determined using the image correlation system (ICS) correlate well with those obtained from electrical strain gauges. However, differences of 38% to 52% were observed between the maximum strain measured with either ICS or electrical strain gages attached to the fiber bundles and the maximum strain in the fiber bundles computed from the maximum applied load. ICS is also used to measure slip and strain of bare fiber bundles, and results show that the load distribution among fiber bundles is non-uniform. The proposed measurement approach shows higher spatial measurement resolution and increased accuracy compared to traditional contact approaches by enabling measurements in each fiber bundle and overcoming the need to attach additional elements to the tested specimen.

Keywords

bond, carbon fiber, digital image correlation, direct shear, FRCM composite, point tracking

1. Introduction and Background

Fiber reinforced cementitious matrix composites have recently been shown great interest by the research community for strengthening of reinforced concrete (RC) and masonry structures. Inorganic cement based matrixes could represent a sustainable and durable alternative to epoxy used in fiber reinforced polymer (FRP) composites. The matrixes are cement based mortars that are usually modified by the addition of fly ash, silica fume, polymers, and/or short, low modulus fibers that improve the strength, bond characteristics, durability, and ultimate deformation of the matrix [1]. The mortar matrix is reinforced with continuous fibers in the form of a unidirectional sheet or a bidirectional net to create the composite. Different names are used for this type of composite including mineral based composites (MBC), textile reinforced mortar (TRM), textile reinforced concrete (TRC), and fiber reinforced cementitious matrix (FRCM) composites. In this paper, the term FRCM composites will be used. Types of fibers commonly used in FRCM composites are carbon, glass, steel, polyparaphenylene benzobisoxazole (PBO), or aramid [2].

Studies reported so far in the literature demonstrate that externally-bonded FRCM composites can be used successfully in RC strengthening applications (e.g., flexure [3-6], shear [7-9], and confinement [10-13]). The bond between the additional reinforcement and the substrate to which it is applied is essential for load sharing. Debonding failures are critical in strengthening applications because loss of composite action can trigger global member failure. Thus, understanding the transfer of force by bond between the FRCM composite and concrete is important for formulating appropriate design models.

The limited available research on the bond behavior of FRCM composites suggests that debonding usually occurs within the matrix as a progressive process at the matrix-fiber interface [14-18], however other failure modes, therefore mechanisms, have been reported throughout the literature such as debonding with cohesive failure in the substrate, debonding at the substrate-matrix interface

[3,8], debonding at the interface between two consecutive layers of matrix [6], and fiber rupture [17]. Accordingly, the bond behavior of FRCM strengthening systems depends on both the bond between the embedded fiber bundles and the matrix, and between the matrix and the concrete surface [19].

The bond behavior of FRP-concrete joints has been studied extensively using direct shear tests [20-25], and more recently this type of test has been used to study the behavior of FRCM composites bonded to concrete (e.g., single-lap [2,14,26], double-lap [27,28]). Direct shear tests of FRCM-concrete joints have been carried out to investigate the load response and failure mode of the bonded composite and to determine key aspects such as the load-carrying capacity of the interface and the interfacial shear stress – slip relation. To do so, contact measurements with traditional sensors such as linear variable displacement transducers (LVDTs) and electrical strain gages have been used to determine the fiber slippage and strain in the longitudinal fibers at pre-determined and discrete locations. For example, several studies have measured the slip at the composite loaded end, termed the "global slip" g, by averaging the displacement readings by LVDTs attached to the concrete surface on either side of the composite and reacting off a plate that is attached to the bare fiber net just outside of the composite loaded end [14,2,26]. Also, axial strain profiles determined by uniaxial electrical resistance strain gages mounted to the longitudinal fibers at discrete locations along the bonded length have been used to determine the effective bond length [27,16,18,2,14] and the debonding load using a fracture mechanics approach [14]. The effective bond length is defined as the minimum bonded length needed to develop the load-carrying capacity of the interface. Strain profiles determined in this manner were also used to determine the fracture energy of the matrix-fiber interface [26,14].

Although direct shear tests are straightforward to carry out, interpretation of the results from a limited number of contact measurements at pre-determined and discrete locations can be challenging considering complex issues such as cracking on the surface of the matrix [29,2,30], non-uniform load distribution among individual fiber bundles [26], and eccentricity between the applied load and supports [31]. Experimental tests on FRCM-concrete joints often show a wide variability in applied load – global slip response [17], and this variability may be related to one or more of the aforementioned factors. Since experimental results are often used in model development and calibration [32-34], it is important that the results from experiments be well-understood.

Digital photogrammetry is a non-contact measuring approach for identifying coordinates of points

and patterns in images obtained using imaging sensors such as charged-coupled devices (CCD) at different stages. Baqersad et al. [35] classified digital photogrammetry techniques based on the targets used as point tracking (PT), digital image correlation (DIC), and targetless approach. In this study only PT and DIC techniques were used. The PT technique identifies the coordinates of discrete points using optical targets mounted to test structures. The optical targets are found using an ellipse finding algorithm within each image. A subpixel edge localization algorithm is used to accurately determine the shape of the ellipse as the generalization of a circle [36]. The coordinates of the center of the fitted ellipse are identified using the triangulation technique. The displacements of the targets are determined by tracking the optical targets in different time stages and comparing their coordinates to the reference (unloaded) stage [35].

DIC is a full field technique that works based on gray-scale variations of a continuous pattern, usually a high contrast stochastic sprayed on pattern. Subsets of an image are identified based on the stochastically distributed image information (i.e. light intensity), and the multi-dimensional displacement of each subset is determined relative to its initial position. The individual displacement of all subsets in an image constitutes the displacement field. DIC has become an accepted method for measuring the surface displacement and displacement gradients in solid mechanics. Currently there are several commercial image correlation systems (ICS) available on the open market. ICS are relatively simple to implement and provide a large range of potential applications [37,38,23]. Additional information on digital photogrammetry is summarized in [35,39].

This paper presents a non-contact measurement approach, based on digital photogrammetry, applied to the experimental study of the bond behavior of fiber reinforced cementitious matrix composite (FRCM) - concrete joints tested in single-lap direct shear tests. The current focus is to develop practical techniques for studying the behavior of bonded FRCM composites that provide more effective and non-ambiguous results in order to aid in the understanding of the stress-transfer mechanism within the composite. The use of ICS and traditional contact measurement (LVDTs and strain gages) approaches are evaluated and discussed. Results of this study are intended to provide a basis and guidance for future studies of the bond behavior of FRCM composites.

2. Experimental campaign

2.1 Materials

The composite was comprised of a bidirectional, balanced, dry carbon fiber net and a cementitious

mortar matrix. Mechanical properties of the fibers are provided in terms of ultimate tensile strength, f_f, 4700 MPa, ultimate tensile strain $\varepsilon_{fu,}$ 1.8%, and modulus of elasticity, E_f, 240 GPa. The fiber net geometrical properties are characterized by the center-to-center bundle spacing, b_f, 20 mm, bundle width, b^*, and bundle thickness t^*. The cross sectional area of the bundles, A_b^*, was determined following the procedure to obtain the linear mass density of bundles indicated in [40]. Assuming a rectangular cross section, t^* was calculated by dividing A_b^* by b^*, assumed to be equal to 5 mm. Based on a sample of six bundles taken from one fiber net, the average value of A_b^* was 1.057 mm^2 with a coefficient of variation (COV) of 0.011. The average value of t^* was 0.210 mm with a COV of 0.055.

The matrix was a ready-mixed, cementitious, shrinkage-compensated, fiber reinforced compound mortar. The mean flexural strength f_{tm} and mean compressive strength f_{cm} of the mortar were determined according to [41] and [42]. Nine 40×40×160 mm prisms were used to determine f_{tm} 6.83 MPa (COV 0.173), and the resulting two halves of each prism were tested in compression between 40×40 mm steel plates to determine f_{cm} 32.8MPa (COV 0.145). The samples were tested at 28 days. The concrete prisms were made of normalweight portland cement concrete with the maximum aggregate size of 10 mm. The mean compressive strength f_c of 59.3 MPa (COV 0.150) was determined according to EN:12390-3 [43] at 28 days with six $150 \times 150 \times 150$ mm cubes.

2.2 Test specimens

Composite strips were cast in place onto the surface of unreinforced concrete prisms. All concrete prisms were $125 \times 125 \times 500$ mm. The fiber strips were 500 mm long containing three longitudinal fiber bundles. The width b of the composite strip was 60 mm, so that three longitudinal fiber bundles of the net would be fully embedded in the matrix. The bonded length used in this study was $l_c = 330$ mm and was chosen based on previous studies indicating the effective bond length of carbon FRCM composite is longer than 200 mm [18]. It should be noted that according to D'Ambrisi et al. [16] the effective bond length of carbon FRCM composite is less than 110 mm. Because of these different results, as a conservative approach a relatively long bonded length was used in this study.

The concrete surface was cleaned and prepared with light sandblasting corresponding to a Concrete Surface Profile number 3, as defined by the International Concrete Repair Institute [44], prior to applying the composite. Wood forms were first attached to the surface of the concrete prism to allow for good control of the bonded area and thickness, then a mortar layer (internal layer) of 4 mm

thickness was cast onto the concrete surface. The fiber net was subsequently placed on the surface of the fresh mortar. A second set of forms was attached on top of the fiber net to secure it in place and to cast the external layer of mortar of 4 mm thickness, resulting in an 8 mm composite thickness. The specimens were then cured in the laboratory under normal ambient conditions (20°C and 50% relative humidity) until the day of testing.

In this paper three specimens are presented and discussed in detail. The specimens presented are part of a larger experimental program that included different fiber types and different ages of composite at test date as presented elsewhere [45]. Each group is identified by acronyms indicating the fiber type (C=carbon) and the age in days of the composite at test date. The identification of a particular specimen in a group is indicated by the last digit (for example, C_28_2 indicates carbon fibers, age at test date of 28 days, second specimen of the series). The same naming system is adopted in this paper for clarity. The three specimens included in this paper are replicate specimens from the same group. The specimens were equipped with a variety of instrumentation (discussed in Section 2.4) so that the results could be examined and compared. The specimens are listed in Table 1.

2.3 Test setup and procedure

A single-lap (direct) shear test setup was adopted in this study. A push-pull configuration was used in which the composite fibers were pulled while the concrete prism was restrained (Fig. 1a). A similar test setup was used by others [46,47,2] to test other FRCM composite-concrete joints. Two aluminum plates were glued to the end of the fiber net using a thermosetting epoxy resin (Fig. 1b,c). The aluminum plates were then introduced between two steel plates that were bolted together to clamp the fiber net. The steel clamp was attached to a pinned joint through which the load was applied to the bare fiber strips. The concrete prism was restrained using a 50 mm thick steel plate anchored with four 18 mm diameter rods to the fixed end of the testing machine.

The loading was applied in displacement (machine stroke) control at a rate of 0.05 mm/min using a closed loop servo-hydraulic universal testing machine with a maximum capacity of 600 kN. The testing machine was equipped with load cell having a 3.75 N absolute resolution and 0.36% expected measuring uncertainty. The load was recorded at frequency of 10 Hz. Data from the testing machine and the instrumentation (discussed in Section 2.4) were acquired by data acquisition systems controlled by personal computers.

2.4 Instrumentation

2.4.1 Non-contact measurements

A commercially available 3D ICS was used in this study. The ICS system contains two 5 Megapixel CCD digital cameras equipped with 12 mm focal length lenses, a data acquisition and storage system, and a dedicated software for data processing and computation of measurements. Images were acquired with a frequency of 1 Hz together with the corresponding load provided by the load cell of the testing machine (Section 2.3). The ICS was used to employ the PT and DIC techniques.

The measuring volume is defined as the 3D space that the ICS system can measure and for which it is calibrated. For the tests in this study, the system was calibrated following the manufacturer's recommendations for a measuring volume of $390 \times 340 \times 340$ mm (width $\times$ height $\times$ depth). The measuring volume contains a cloud of uniquely identified measuring points, with a set of 3D Cartesian coordinates (x,y,z). In this study, the origin of the Cartesian coordinate system was chosen at bottom left corner of the composite as shown in Fig. 1b,c.

In this work the PT technique was used to evaluate displacement and strain of the composite fiber bundles via virtual displacement transducers and virtual strain gages described in the paragraphs that follow, while the DIC technique was used to evaluate the displacement and strain fields on the surface of the matrix. Optical targets used for the PT technique were high contrast adhesive markers with a defined circular geometry and 1.5 mm diameter (Fig. 1c). For DIC measurements, a white base layer was applied to the surface of the specimen, and then black paint was sprayed using an airbrush to create a high contrast, random speckle pattern required for DIC (Fig. 1a, 1c).

Virtual displacement transducers (VDTs) were defined and used to determine the global slip of individual longitudinal fiber bundles g_i (subscript i=1,2,3 denotes the bundle numbered from left to right on the front of the specimen). g_i is measured as the change in distance between the measuring point on the corresponding fiber bundle and a reference line defined by Reference Point 1 and Reference Point 2 located on the top support steel plate that is assumed to be fixed throughout the test. In Fig. 2, three VDTs are defined from left to right with a number identifying the longitudinal fiber bundle and are named VDT1, VDT2, and VDT3.

Virtual strain gages (VSGs) were defined and used to measure strain in the individual longitudinal fiber bundles by determining the relative change in distance between two point markers attached to the fiber bundles. In this case strain is defined as a change in the distance between two measuring

points on the bundle divided by the initial distance between them, referred to as the gauge length. Three VSGs are shown in Fig. 3 as ε_i^v. VSGs ε_1^v, ε_2^v, and ε_3^v were used to measure the strain between point markers 10 and 11, 20 and 21, and 30 and 31, respectively, shown in Fig. 3.

DIC results were obtained using a 10 pixel facet size at a step of 10 pixels. This choice of facet and step size showed suitable resolution and accuracy, similar to results presented by D'Antino et al. [31]. The measurement accuracy of the ICS system was 0.037 pixels. For the measuring volume used, a displacement accuracy of 0.006 mm and a strain accuracy of 1000 με was obtained. Measurements acquired by ICS for each specimen are summarized in Table 1.

2.4.2 Contact measurements

For one specimen (specimen C_28_2), the global slip g was measured using two LVDTs, D1 and D2 (Fig. 1b), that were attached to the concrete surface close to the composite edge and oriented parallel to the bonded length. The rod of the LVDTs reacted against an aluminum L-plate that was glued to the bare fiber net outside of the bonded area. The average of the two LDVT measurements is reported as $\bar{g}$.

Two specimens (specimens C_28_2 and C_28_3) were instrumented with five uniaxial electrical strain gages $\varepsilon_{i,j}$, with subscript i denoting the fiber bundle and subscript j denoting the location of the strain gage on the fiber bundle as shown in Fig. 1. The strain gages were attached to the longitudinal fiber bundle using a cyanoacrylate adhesive prior to casting the composite.

Measurements acquired by the LVDTs and electrical strain gages for each specimen are summarized in Table 1. Measurements from the LVDTs and electrical strain gages were sampled at a frequency of 10 Hz.

3. Experimental results

3.1 General behavior, failure mode, and maximum load

For each of the specimens presented in this paper, failure was characterized by considerable slippage between the fibers and matrix. Debonding occurred at the fiber-matrix interface, and no damage was observed at the matrix-concrete interface.

Cracking of the matrix was observed on the composite surface of specimens C_28_2 and C_28_3 at the locations of electrical strain gages $\varepsilon_{2,2}$ and $\varepsilon_{2,3}$ after the maximum load. Cracking was likely caused by a stress concentration due to the presence of the strain gauge [2] and large slips between

the fibers and the substrate accompanied by eccentricity in the applied load [31]. Matrix cracking is discussed further in Section 4.4.

The normal stress σ_P and strain ε_P in the longitudinal fiber bundles associated with the applied load P are defined by Equation 1 and Equation 2, respectively:

$$\sigma_P = \frac{P}{nA_b^*} \qquad \text{Equation 1}$$

$$\varepsilon_P = \frac{\sigma_P}{E_f} \qquad \text{Equation 2}$$

where n is the number of longitudinal fiber bundles (n=3). It should be noted that in Equations 1 and 2, σ_P and ε_P are calculated assuming the load is shared evenly between the bundles in the composite and that the stress distribution over the bundle cross section is uniform. Although previous studies [26] and [48] have demonstrated that these two assumptions do not hold, similar equations are often used to compare composites with different widths [28,14] or different fiber-to-matrix reinforcement ratios and have also been proposed within procedures to provide engineering parameters for externally bonded FRCM reinforcement [17,49].

Table 1 reports the maximum load P_{max}, the average global slip at the maximum load $\bar{g}_i^{P_{max}}$ computed as the average of the slip measured on each fiber bundle g_i (measured using ICS), the average global slip at maximum load $\bar{g}^{P_{max}}$ computed as the average of the two LVDT measurements (specimen C_28_2 only), the normal stress in the longitudinal fiber bundles at the maximum load $\sigma_P^{P_{max}}$ determined by Equation 1, the strain in the fibers at the maximum load $\varepsilon_P^{P_{max}}$ determined by Equation 2, the strain in the central fiber bundle measured by ICS ε_2^v at the maximum load $\varepsilon_2^{v,P_{max}}$, the strain in the central fiber bundle measured by electrical strain gauge $\varepsilon_{2,1}$ at the maximum load $\varepsilon_{2,1}^{P_{max}}$ (specimens C_28_2 and C_28_3), and the observed failure mode.

3.2 Load-global slip response

The applied load P – global slip responses for the three specimens are shown in Fig. 4 in which the global slip of each individual fiber bundle g_i determined using ICS is plotted. Fig. 4 also plots the average global slip, $\bar{g}_i$ determined as the average of the slip measured on each fiber bundle g_i for each load level. The responses in Fig. 4 show that each specimen exhibits an initial linear response. After a certain load level the response becomes non-linear. After the maximum load is reached, the applied load decreases with increasing global slip until a constant value of P is reached. The load

responses resemble the idealized response described by D'Antino et al. [14] for PBO FRCM-concrete joints.

For a given load level, Fig. 4 shows that measurements of global slip in individual fiber bundles g_i are generally consistent for specimens C_28_2 and C_28_3 up to the maximum load. On the other hand, measurements of global slip in individual fiber bundles are significantly different for a given load level for specimen C_28_1, which shows a sudden change in stiffness at a maximum load of 0.779 kN. This is believed to be caused by a non-uniform distribution of load between the longitudinal fiber bundles and is discussed further in Section 4.2. This behavior was observed by other researchers in single-lap shear tests of FRCM-concrete joints using contact measurements [2].

3.3 Longitudinal fiber strain profiles

The variation of axial strain ε_{yy} along the length of the central longitudinal fiber bundle measured with electrical strain gages at different values of applied load P is presented Fig. 5a and b for specimens C_28_2 and C_28_3, respectively. The axes and strain gage positions are defined in Fig. 1. The strains measured outside of the bonded length at the maximum load P_{max} ($\varepsilon_{2,1}^{P_{max}}$) were 5680 $\mu\varepsilon$ and 4870 $\mu\varepsilon$ for specimens C_28_2 and C_28_3, respectively (see Table 1).

In the profiles shown in Fig. 5, the strain in the fiber bundles was considered constant over the length from the location of $\varepsilon_{2,1}$ (y=377 mm) to the beginning of the bonded area (y=330 mm). This assumption is supported by findings reported in [2] on PBO FRCM-concrete joints instrumented with electrical strain gages placed in additional locations along the bare fibers outside the bonded area.

Axial strains determined with ICS on the central fiber bundle of specimen C_28_3 outside the bonded region, ε_2^v, are also plotted in Fig. 5b at the corresponding location y for the same load levels as those used to plot the electrical strain gage readings. Values of ε_2^v determined with ICS show good correlation with values determined by electrical strain gage $\varepsilon_{2,1}$ (i.e., within 5%).

The value of strains measured with the electrical strain gauge on the central bundle outside the bonded region at the maximum load $\varepsilon_{2,1}^{P_{max}}$, as well as the value determined by ICS $\varepsilon_2^{v,P_{max}}$ for specimen C_28_3, are considerably higher than the value $\varepsilon_P^{P_{max}}$ computed using Equations 1 and 2 for applied load $P = P_{max}$ (see Table 1). A similar observation was made other authors [27,16] and was attributed to the non-uniform strain distribution among fibers within a single bundle. However, the difference

between $\varepsilon_P^{P_{max}}$ and values of $\varepsilon_{2,1}^{P_{max}}$ and $\varepsilon_2^{v,P_{max}}$ can also be attributed to the non-uniform load distribution between the longitudinal fiber bundles as further demonstrated in Section 4.2.

The strain profiles plotted in Fig. 5 suggest that the effective bond length of the carbon-FRCM composite is longer than 200 mm but less than 330 mm. This is in good agreement with results of Malena et al. [18], who reported an effective transfer length of approximately 200 mm, and is different than results of D'Ambrisi et al. [16] who reported an effective anchorage length lower than 110 mm. It should be noted that both results of [18] and [16] were obtained using masonry substrates, however debonding was associated with slippage of the fibers relative to the matrix, as in the case of the present study.

The axial strain profiles in Fig. 5a for specimen C_28_2 (with an L-plate used to measure g with the LDVTs) show a decrease in strain along the bundle length from $\varepsilon_{2,2}$ ($y = 277$ mm) to the location of $\varepsilon_{2,1}$ ($y = 377$ mm) at load levels close to the maximum load. Strain fluctuations close to the loaded end were also reported by Sneed et al. [2] at load levels close to the maximum load, followed by a sharp increase in recorded strain after considerable slip, which was attributed to local bond conditions and debonding of the electrical strain gage caused by large slips. However, such behavior was not observed in this study. It is possible that the attached L-plate plays a role in the load distribution between the bundles, in this case concentrating more load in the central bundle. Further studies are required to study this issue, where the strain along the length of each fiber bundle should be measured.

3.4 Matrix surface strain and displacement field

The ICS system was used to obtain the displacement and strain fields on the surface of the specimens by means of the DIC method. Fig. 6a and c show the axial strain ε_{yy} profile on the surface of the composite along the composite bonded length at the maximum load for specimens C_28_2 and C_28_3, respectively. The longitudinal strains ε_{yy} were computed as the average over the range from 4.0 mm < x < 9.0 mm, where x = 7.5 mm corresponds to the center of the left bundle (bundle 1). The left bundle was chosen for this analysis because the presence of wires connecting the electrical strain gages to the data acquisition system interfered with the images of the ICS system over the center and right bundle.

Fig. 6a and c show that the values of axial strain on the external surface of the composite were relatively small ($\pm$ 1000 $\mu\varepsilon$) and are much smaller than values measured in the central fiber bundle

at various positions y along the composite bonded length of the same specimen (Fig. 5a and b, respectively). As noted in [2], in the case of FRCM composites values of strain must be determined on the fibers instead of the composite surface, as is common in the case of FRP. This issue presents a challenge in determining the strain profiles using ICS, since measurements are taken on the surface of the body, however one possible approach is the method described by Carloni et al. [26] where the external matrix layer was omitted thereby exposing the fiber net.

Fig. 6a and also show the longitudinal displacement d_{yy} of the matrix surface at $x = 7.5$ mm obtained by DIC for different values of $\bar{g}_i$ for specimens C_28_2 and C_28_3, respectively. The applied load P – average global slip $\bar{g}_i$ relations for the corresponding specimens are shown in Fig. 6b and d, respectively, for comparison. Fig. 6a and c show that at the average global slip corresponding to the maximum load, very small values of longitudinal displacement were measured along the surface of the composite. As the average global slip was increased, portions of the matrix surface near the loaded end showed non-zero displacement measurements that increased in magnitude and length in a step-wise manner with increasing values of global slip. Further discussion on the surface displacements is presented in Section 4.4.

4. Discussion

4.1 Comparison of load responses determined by LDVT and ICS measurements

The top part of Fig. 7 shows the applied load-global slip response of specimen C_28_2 in which the dashed lines represent the displacement measurements of the individual LVDTs, and the solid lines represent the global slip of each bundle measured with ICS. The use of LVDTs reacting off the L-plate glued on the bare fibers yielded values that were initially negative caused by the rotation of the L-plate about the x-axis (i.e., out-of-plane of the composite). Because the bare fiber net is flexible, when the bundles are not tensioned, the spring in the two LVDTs is strong enough to cause the rotation of the L-plate at the initial stage. Together with the increase of the applied load P, the bundles straighten as a result of tensioning. This in turn rotates the L-plate back, perpendicular to the fiber net, causing negative readings of LVDTs as shown by the plots of D1raw and D2raw. After a load level of P=0.8 kN it was observed that the L-plate stabilized, and the LVDT measurements were adjusted to zero. The adjusted curves are shown as D1 and D2. The correction can be

considered equivalent to pretensioning the fibers at the beginning of the test. It should be noted that details about such specimen preparation or adjustments are not commonly reported in the available literature. Also, several types LVDT-plate assemblies have been used in single lap direct shear tests of FRCM-concrete joints [2,17,46], however it is not discussed if such effects were observed.

On the other hand, measurements with ICS did not appear to be influenced by the rotation of the L-plate at the beginning of the test. The ICS-measured slip of each fiber bundle is shown by the g_1, g_2, and g_3 curves, which are similar to the D1 and D2 (corrected) curves.

The bottom part of Fig. 7 compares the applied load P – global slip $\bar{g}_{raw}$ response, obtained by averaging the values of D1raw and D2raw, and the P - global slip $\bar{g}$ response, obtained by averaging the D1 and D2 values, to the applied load P – global slip $\bar{g}_i$ response, obtained by averaging $\bar{g}_1$, $\bar{g}_2$, and $\bar{g}_3$. It can observed that the P - $\bar{g}$ and P - $\bar{g}_i$ responses are similar in shape, although the P - $\bar{g}$ response shows a higher initial rigidity compared to the P - $\bar{g}_i$ response. This is believed to be the result of the initial prestress and rotation of the L-plate around the x-axis. Therefore the initial rigidity is slightly overestimated when using measurements from the LVDTs. These results suggest that ICS measurements are able to capture better the initial load response of FRCM – concrete joints. The onset of the nonlinear response of the joint can be more easily identified and the scatter observed in the linear response [17,32,33] can be reduced.

4.2 Load distribution between fiber bundles

The impregnation of the matrix into the fiber bundles of FRCM composites can differ from bundle to bundle causing the applied load to be shared unevenly between the bundles. The non-uniform load distribution was evidenced and studied by Carloni et al. [26] by a rigid rotation of the plate attached to the bare fiber bundles used to measure g, however the discrete distribution of the load among the different fiber bundles could not be quantified in that study.

In specimen C_28_2 the non-uniform distribution of the load is evidenced in Fig. 7 by the difference in the D1 and D2 curves, determined by the two LVDT measurements. A similar non-uniform distribution can be observed from the difference in g_1, g_2, and g_3 curves of the ICS measurements.

Individual measurements g_i on each bundle also show that the load distribution among the bundles is not linear across the width of the composite. Instead it is influenced by the random nature of the bonding properties between the fibers and matrix. The load distribution can be better observed on specimen C_28_1 (Fig. 4) where, due to a more pronounced non-uniformity of the load, the

13

specimen failed prematurely. In specimen C_28_1 one bundle (bundle 3, corresponding to g_3) appeared to have better bond with the matrix than the other two bundles. This explains the high discrepancy in the maximum loads between specimen C_28_1 and specimens C_28_2 and C_28_3 (Table 1).

Using ICS, the strain in each bare fiber bundle ε_i^v can be associated to the global slip of each bundle g_i. Fig. 8 shows the $\varepsilon_i^v - g_i$ behavior of the three longitudinal bundles for specimen C_28_3. For comparison, the $\varepsilon_{2,1}$- g_2 response is also plotted in the graph where $\varepsilon_{2,1}$ is the value determined by the electrical strain gage mounted outside the bonded region (see Fig. 1c). The measured response of bundle 2 using the electrical strain gage $\varepsilon_{2.1}$ and ICS ε_2^v shows good agreement. The strain ε_2^v measured with ICS shows higher noise than the strain measured with the electrical strain gage $\varepsilon_{2,1}$. The accuracy of ε_i^v can be increased by using an ICS with higher camera resolution or longer gage length.

In Fig. 8 it can be observed that all bundles attain similar maximum strains (i.e., between 4850 and 5700 με), however the overall pullout behavior of the different bundles is significantly different. For reference, the global slip measured in each bundle at the maximum load g_i^{Pmax} is indicated by dashed lines in the figure. Fig. 8 shows that at maximum load (as indicated by the corresponding values of g_i^{Pmax}), the strain level in the bundles varies substantially (i.e., values of ε_1^v, ε_2^v, and ε_3^v are 1587 με, 4990 με, and 3994 με, respectively). The responses also show that the debonding process of the individual fiber bundles can start before the maximum load is reached (bundles 1 and 3) or after (bundle 2). These results obtained by ICS exemplify the non-uniform distribution of the applied load between the bundles based on the measured strain. The authors assume that the non-uniform load distribution is a result of stochastically distributed bond properties between the fiber bundles and the matrix that influence the axial stiffness of the bundle, despite the load being applied uniformly to the bundles through the epoxy bonded aluminum plates. In the case of specimen C_28_3, cracking of the matrix was not observed until later in the debonding process, which suggests that although cracking can influence the load distribution between the bundles, there are other reasons why the load is not uniformly distributed, even in the apparently elastic part of the response.

4.3 Longitudinal fiber bundle strain

Strains in the longitudinal fiber bundles in FRCM composites have been shown to vary across the cross section of the bundle [48]. Because the matrix cannot fully penetrate in between the fibers of

the bundle, the fibers in the outside sleeve are more heavily stressed than the fibers in the core of the bundle. The bare fibers bundles outside the composite bonded area (from y=330 mm up to the clamped end) are expected to have this same distribution across the cross section of the bundle.

As mentioned in Section 2.4.1, the point markers used to define the VSGs were self-adhesive stickers attached the surface of the bundle (to the fibers in the outer layer of the bundle) (Fig. 1c). If the assumption that the strain in the outer layer of fibers of a bundle as defined in [48] is constant holds, then the strain measured using VSGs represents the strain in the outer layer (sleeve), and is therefore expected to be larger than the average strain in the fiber bundle. On the other hand, electrical strain gages were glued to the fiber bundle using a cyanoacrylate adhesive with a relatively low viscosity. Besides bonding the electrical strain gage to the fibers, the adhesive impregnates the bundle and bonds the fibers together, possibly influencing the local stress distribution over the bundle cross section and the debonding of the bundle from the matrix. However, the typical tensile modulus of cyanoacrylate adhesive is 1.2 GPa, therefore the influence can be considered small, and the strain measured by electrical strain gages can be assumed to be the strain in the outer sleeve of the bundle. The good correlation between the strains measured outside the composite bonded region with ICS and the electrical strain gages in Fig. 5b confirms the assumption that the strain measured with strain gages is indeed the strain in the bundle outer sleeve fibers.

Differences of 38% to 52% were observed between the values of maximum strain in fiber bundles obtained from the maximum applied load and values measured with either electrical strain gages attached to the fiber bundle or using the ICS. On the other hand, results of Sneed et al. [2] show that the strain measured with strain gages coincides with the computed average strain in the bundle based on the applied load suggesting that glued-on strain gages provide the average strain in the bundle rather than the strain in the outer sleeve bundles. However, the results in that study were obtained based on measurements from only one bundle of the composite and could be influenced by the previously discussed non-uniform load distribution load between the bundles.

4.4 Significance of matrix surface strain and displacement measurements

The matrix surface strains depicted in Fig. 6a and c show oscillations with a maximum amplitude of 1000 $\mu\varepsilon$. In the study by D'Antino et al. [31] oscillations of similar nature and magnitude were observed and attributed to the presence of the transversal bundles of the fiber net. According to

Mazzoleni [50], DIC presents higher uncertainties for constant displacement fields (zero strain), and the uncertainty decreases with the increase of deformation. For the measuring volume used in this case, strains below 1000 $\mu\varepsilon$ are below the system's measurement noise level, and therefore Fig. 6a and c indicate a zero strain state on the matrix surface. The assumption of a zero strain state on the matrix surface is confirmed by the constant displacement fields depicted in Fig. 6a and c and is in good agreement with findings of D'Antino et al. [31] showing a rigid body motion of the external matrix layer. However increasing the measuring accuracy or changing the measurement field size could possibly lead to different results.

After the maximum load, at a global slip value $\bar{g}_i$ of 1.60 and 1.70 mm for specimens C_28_2 and C_28_3, respectively, cracks appeared on the matrix surface spanning across the composite width on both specimens. Cracks appeared when the strain in the matrix exceeded the ultimate tensile strain of the mortar. The presence of strain gages most likely resulted in local stress concentrations in the matrix at large values of slip. The formation of cracks is shown in Fig. 6a and c as a sharp increase in the longitudinal displacement indicating their location along the bonded length. At $\bar{g}_i =$ 3.60 mm for both specimens two cracks and their locations can be observed in Fig. 6a and c. Fig. 6a and c also show that the displacement field between the cracks is constant suggesting rigid body motion of the segments of the external matrix layer.

In general the load response of the FRCM-concrete joint is influenced by the presence of cracks in the matrix [31]. In Fig. 6 it can be observed that the formation and opening of the first crack is associated with a sudden drop in the applied load. Since the first crack appears after the maximum load, the stress transfer mechanism between the fiber bundles and the matrix up to maximum load is not affected for the specimens considered.

5. Conclusions

A non-contact measurement approach based on digital photogrammetry, applied to the experimental study of the bond behavior of fiber reinforced cementitious matrix (FRCM) - concrete joints by single-lap direct shear tests, was presented in this paper. The tests were carried out in a universal testing machine and instrumented with both traditional contact measurement systems (LVDTs and electrical strain gages) and state-of-the-art non-contact ICS (including PT and DIC techniques). A method using a commercially available ICS to measure the global slip g and strain in the bare fiber bundles at the loaded end was proposed. Based on the results of this study and discussions

16

concerning contact and non-contact measuring methods presented herein, the following conclusions can be made:

- The strain in the bare fiber bundles at the loaded end measured using ICS (PT method) showed good correlation with the measurements obtained from electrical strain gages;

- Using the ICS (PT method) the load - global slip response of each individual fiber bundle, and of the FRCM –concrete joint, can be determined with a higher accuracy compared to LVDTs and overcome the need to attach additional elements to the tested specimen;

- ICS results demonstrated that in single-lap direct-shear setups, the applied load is not distributed uniformly to the fiber bundles but rather is randomly distributed based on the bond properties of each bundle;

- Differences of 38% to 52% were observed between the values of maximum strain in fiber bundles computed from the maximum applied load and values measured with either electrical strain gages attached to the fiber bundle or using ICS (PT method). These results show that approximating the strain in the fiber from the maximum load may not be representative of the actual strain in the fiber bundles, and can even yield to erroneous results;

- Crack detection and localization in the composite matrix was determined using DIC. Sudden drops in the applied load were shown to be correlated with the formation of cracks;

- Debonding of the carbon-FRCM composite in this study occurred at the matrix-fiber interface. The axial strain distribution along the bundle length suggests an effective bond length between 200 mm and 330 mm.

While the results presented in this study are based on a limited number of specimens, the authors believe that the advantages of digital photogrammetry (especially the point tracking method) over contact instruments discussed herein can greatly aid the study of the complex behavior of FRCM-concrete joints in future experimental tests.

References

1. Orosz K, Blanksvärd T, Täljsten B, Fischer G (2010) From Material Level to Structural Use of Mineral-Based Composites—An Overview. Advances in Civil Engineering 2010:1-19. doi:10.1155/2010/985843

2. Sneed LH, D'Antino T, Carloni C (2014) Investigation of Bond Behavior of Polyparaphenylene Benzobisoxazole Fiber-Reinforced Cementitious Matrix Composite-Concrete Interface. ACI Materials Journal 111 (5):569-580. doi:10.14359.51686604

3. Täljsten B, Blanksvärd T (2007) Mineral-Based Bonding of Carbon FRP to Strengthen Concrete Structures. Journal of Composites for Construction 11 (2):120-128. doi:10.1061/(ASCE)1090-0268(2007)11:2(120)

4. D'Ambrisi A, Focacci F (2011) Flexural Strengthening of RC Beams with Cement-Based Composites. Journal of Composites for Construction 15 (5):707-720. doi:10.1061/(asce)cc.1943-5614.0000218

5. Elsanadedy HM, Almusallam TH, Alsayed SH, Al-Salloum YA (2013) Flexural strengthening of RC beams using textile reinforced mortar – Experimental and numerical study. Composite Structures 97 (0):40-55. doi:10.1016/j.compstruct.2012.09.053

6. Sneed LH, Verre S, Carloni C, Ombres L (2016) Flexural behavior of RC beams strengthened with steel-FRCM composite. Engineering Structures 127:686-699. doi:10.1016/j.engstruct.2016.09.006

7. Triantafillou TC, Papanicolaou CG (2006) Shear strengthening of reinforced concrete members with textile reinforced mortar (TRM) jackets. Mater Struct 39 (1):93-103. doi:10.1617/s11527-005-9034-3

8. Blanksvärd T, Täljsten B, Carolin A (2009) Shear Strengthening of Concrete Structures with the Use of Mineral-Based Composites. Journal of Composites for Construction 13 (1):25-34. doi:10.1061/(ASCE)1090-0268(2009)13:1(25)

9. Al-Salloum YA, Elsanadedy HM, Alsayed SH, Iqbal RA (2012) Experimental and Numerical Study for the Shear Strengthening of Reinforced Concrete Beams Using Textile-Reinforced Mortar. Journal of Composites for Construction 16 (1):74-90. doi:10.1061/(asce)cc.1943-5614.0000239

10. Ortlepp R, Lorenz A, Curbach M (2009) Column Strengthening with TRC: Influences of the Column Geometry onto the Confinement Effect. Advances in Materials Science and Engineering. doi:10.1155/2009/493097

11. Colajanni P, De Domenico F, Recupero A, Spinella N (2014) Concrete columns confined with fibre reinforced cementitious mortars: Experimentation and modelling. Construction and Building Materials 52:375-384. doi:10.1016/j.conbuildmat.2013.11.048

12. Ombres L (2014) Concrete confinement with a cement based high strength composite material. Composite Structures 109:294-304. doi:10.1016/j.compstruct.2013.10.037

13. Ombres L, Verre S (2015) Structural behaviour of fabric reinforced cementitious matrix (FRCM) strengthened concrete columns under eccentric loading. Composites Part B-Engineering 75:235-249. doi:10.1016/j.compositesb.2015.01.042

14. D'Antino T, Carloni C, Sneed LH, Pellegrino C (2014) Matrix-fiber bond behavior in PBO FRCM composites: A fracture mechanics approach. Engineering Fracture Mechanics 117:94-111. doi:10.1016/j.engfracmech.2014.01.011

15. Alecci V, De Stefano M, Luciano R, Rovero L, Stipo G (2016) Experimental Investigation on Bond Behavior of Cement-Matrix-Based Composites for Strengthening of Masonry Structures. Journal of Composites for Construction 20 (1):10. doi:10.1061/(asce)cc.1943-5614.0000598

16. D'Ambrisi A, Feo L, Focacci F (2013) Experimental and analytical investigation on bond between Carbon-FRCM materials and masonry. Composites Part B-Engineering 46:15-20. doi:10.1016/j.compositesb.2012.10.018

17. Ascione L, de Felice G, De Santis S (2015) A qualification method for externally bonded Fibre Reinforced Cementitious Matrix (FRCM) strengthening systems. Composites Part B: Engineering 78:497-506. doi:10.1016/j.compositesb.2015.03.079

18. Malena M, de Felice G (2014) Debonding of composites on a curved masonry substrate: Experimental results and analytical formulation. Composite Structures 112:194-206. doi:10.1016/j.compstruct.2014.02.004

19. Carloni C, Bournas D, Carozzi G, D'Antino T, Fava G, Focacci F, Giacomin G, Mantegazza G, Pellegrino C, Perinelli C, Poggi C (2016) Fiber Reinforced Composites with Cementitious (Inorganic) Matrix. In: Sena-Cruz. CPaJ (ed) Design Procedures for the Use of Composites in Strengthening of Reinforced Concrete Structures, vol RILEM State-of-the-Art Reports 19. RILEM, pp 349-391

20. Taljsten B (1997) Defining anchor lengths of steel and CFRP plates bonded to concrete. International Journal of Adhesion and Adhesives 17 (4):319-327. doi:10.1016/s0143-7496(97)00018-3

21. Carrara P, Ferretti D, Freddi F, Rosati G (2011) Shear tests of carbon fiber plates bonded to concrete with control of snap-back. Engineering Fracture Mechanics 78 (15):2663-2678. doi:10.1016/j.engfracmech.2011.07.003

22. Hadigheh SA, Gravina RJ, Setunge S (2015) Identification of the interfacial fracture mechanism in the FRP laminated substrates using a modified single lap shear test set-up. Engineering Fracture Mechanics 134:317-329. doi:10.1016/j.engfracmech.2014.12.001

23. Czaderski C, Soudki K, Motavalli M (2010) Front and Side View Image Correlation Measurements on FRP to Concrete Pull-Off Bond Tests. Journal of Composites for Construction 14 (4):451-463. doi:10.1061/(ASCE)CC.1943-5614.0000106

24. Subramaniam KV, Carloni C, Nobile L (2007) Width effect in the interface fracture during shear debonding of FRP sheets from concrete. Engineering Fracture Mechanics 74 (4):578-594. doi:10.1016/j.engfracmech.2006.09.002

25. Grace C, Yang Y, Sneed L (2012) Fracture Mechanics Approaches to Debonding Behavior of Reinforced Concrete Members with Externally-bonded Fiber Reinforced Polymer Laminates. ACI Special Publication 286. doi:10.14359/51683907

26. Carloni C, D'Antino T, Sneed L, Pellegrino C (2014) Role of the Matrix Layers in the Stress-Transfer Mechanism of FRCM Composites Bonded to a Concrete Substrate. Journal of Engineering Mechanics 141 (6):04014165. doi:10.1061/(ASCE)EM.1943-7889.0000883

27. D'Ambrisi A, Feo L, Focacci F (2013) Experimental analysis on bond between PBO-FRCM strengthening materials and concrete. Composites Part B: Engineering 44 (1):524-532. doi:10.1016/j.compositesb.2012.03.011

28. Sneed LH, D'Antino T, Carloni C, Pellegrino C (2015) A comparison of the bond behavior of PBO-FRCM composites determined by double-lap and single-lap shear tests. Cement and Concrete Composites 64:37-48. doi:10.1016/j.cemconcomp.2015.07.007

29. Colombo IG, Magri A, Zani G, Colombo M, di Prisco M (2013) Textile Reinforced Concrete: experimental investigation on design parameters. Mater Struct 46 (11):1933-1951. doi:10.1617/s11527-013-0017-5

30. D'Antino T, Sneed LH, Carloni C, Pellegrino C (2015) Influence of the substrate characteristics on the bond behavior of PBO FRCM-concrete joints. Construction and Building Materials 101:838-850. doi:10.1016/j.conbuildmat.2015.10.045

31. D'Antino T, Sneed LH, Carloni C, Pellegrino C (2016) Effect of the inherent eccentricity in single-lap direct-shear tests of PBO FRCM-concrete joints. Composite Structures 142:117-129. doi:10.1016/j.compstruct.2016.01.076

32. Carozzi FG, Milani G, Poggi C (2014) Mechanical properties and numerical modeling of Fabric Reinforced Cementitious Matrix (FRCM) systems for strengthening of masonry structures. Composite Structures 107:711-725. doi:10.1016/j.compstruct.2013.08.026

33. Carozzi FG, Colombi P, Fava G, Poggi C (2016) A cohesive interface crack model for the matrix–textile debonding in FRCM composites. Composite Structures 143:230-241. doi:10.1016/j.compstruct.2016.02.019

34. Carloni C, D'Antino T, Sneed LH, Pellegrino C An Investigation of PBO FRCM-Concrete Joint Behavior using a Three-Dimensional Numerical Approach. In: Kruis J, Tsompanakis Y, Topping BHV (eds) Fifteenth International Conference on Civil, Structural and Environmental Engineering Computing (CC2015), Prague, Czech Republic, 2015. p 15

35. Baqersad J, Poozesh P, Niezrecki C, Avitabile P (2016) Photogrammetry and optical methods in structural dynamics – A review. Mechanical Systems and Signal Processing. doi:10.1016/j.ymssp.2016.02.011

36. Canny J (1986) A Computational Approach to Edge Detection. IEEE Transactions on Pattern Analysis and Machine Intelligence PAMI-8 (6):679-698. doi:10.1109/TPAMI.1986.4767851

37. McCormick N, Lord J (2010) Digital Image Correlation. Materials Today 13 (12):52-54. doi:10.1016/S1369-7021(10)70235-2

38. Ghorbani R, Matta F, Sutton MA (2015) Full-Field Deformation Measurement and Crack Mapping on Confined Masonry Walls Using Digital Image Correlation. Experimental Mechanics 55 (1):227-243. doi:10.1007/s11340-014-9906-y

39. Xiao Z, Liang J, Yu D, Tang Z, Asundi A (2010) An accurate stereo vision system using cross-shaped target self-calibration method based on photogrammetry. Optics and Lasers in Engineering 48 (12):1252-1261. doi:10.1016/j.optlaseng.2010.06.006

40. ASTM:D1577 (2012) Standard Test Methods for Linear Density of Textile Fibers. ASTM International, West Conshohocken, PA, United States

41. ASTM:C348 (2014) Standard Test Method for Flexural Strength of Hydraulic-Cement Mortars. ASTM International, West Conshohocken, PA, United States

42. ASTM:C349 (2014) Standard Test Method for Compressive Strength of Hydraulic-Cement Mortars (Using Portions of Prisms Broken in Flexure). ASTM International, West Conshohocken, PA, United States

43. EN:12390-3 (2009) Testing hardened concrete – Part 3: Compressive strength of test specimens. European Committee for Standardization, Brussels, Belgium

44. ICRI (1997) Selecting and spedifying concrete surface preparation for sealers, coatings, and polymer overlays. Technical Guideline No. 03732, International Concrete Repair Institute, Rosemont, IL, United States

45. Sabau C, Gonzalez-Libreros J, Sneed L, Sas G, Pellegrino C (2016) Influence of fiber type on the bonding behavior of FRCM composite strips applied to concrete substrates. Paper presented at the 8th International Conference on FRP Composites in Civil Engineering, Hong Kong

46. D'Antino T, Pellegrino C, Carloni C, Sneed LH, Giacomin G (2015) Experimental analysis of the bond behavior of glass, carbon, and steel FRCM composites. Key Engineering Materials, vol 624. doi:10.4028/www.scientific.net/KEM.624.371

47. D'Antino T (2014) Bond behavior in fiber reinforced composites and fiber reinforced cemetitious matrix composites. Doctoral Thesis University of Padova, Padova, Italy

48. Banholzer B (2006) Bond of a strand in a cementitious matrix. Mater Struct 39 (10):1015-1028. doi:10.1617/s11527-006-9115-y

49. AC434 (2011) Acceptance criteria for masonry and concrete strengthening using fiber-reinforced cementitious matrix (FRCM) composite systems. ICC Evaluation Service, Birminghan, AL 35213, United States

50. Mazzoleni P (2013) Uncertainty estimation and reduction in digital image correlation measurements. Doctoral thesis, Polytechnic Univ. of Milan, Milan, Italy

Tables

Table 1 Summary of instrumentation and test results

Specimen	Results								Instrumentation				
	P_{max}	$\bar{g}_i^{P_{max}}$	$\bar{g}^{P_{max}}$	$\sigma_P^{P_{max}}$	$\varepsilon_P^{P_{max}}$	$\varepsilon_2^{v,Pmax}$	$\varepsilon_{2,1}^{P_{max}}$	Failure mode	LVDT g	Electrical strain gages $\varepsilon_{i,j}$	ICS		
											VDT g_i	VSG ε_i^v	Matrix strain and displacement field
	[kN]	[mm]	[mm]	[MPa]	[µε]	[µε]	[µε]						
C_28_1	0.779	0.738	-	246	1020	1250	-	FD[a]	✗	✗	✓	✓	✓
C_28_2	1.634	1.073	0.809	515	2150	-	5680	FD[a]	✓	✓	✓	✗	✓
C_28_3	1.947	1.150	-	614	2560	4990	4870	FD[a]	✗	✓	✓	✓	✓

Symbols ✓ and ✗ indicate whether measurements were acquired or not, respectively.
[a]fiber debonding

List of figures

Fig. 1 Test setup (a) photo, (b) and (c) schematic showing locations of LVDTs (D1 and D2), strain gages, point markers, and optical measurements for specimens C_28_2 and C_28_3, respectively (g_i denotes the location of global slip measurement on fiber bundle; $\varepsilon_{i,j}$ denotes electrical strain gage; ε_i^y denotes virtual strain gage on the fiber bundle)
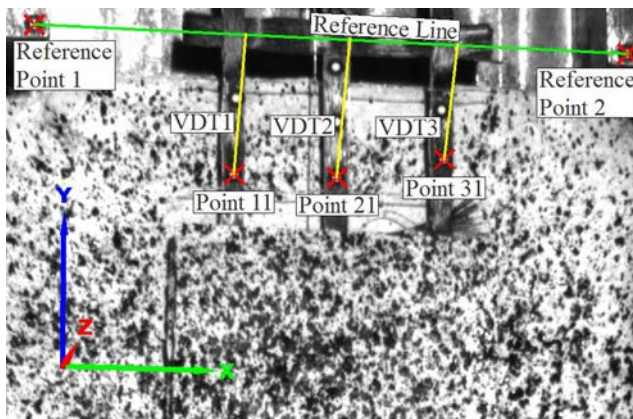

Fig. 2 Definition of virtual displacement transducers (VDTs), specimen C_28_3
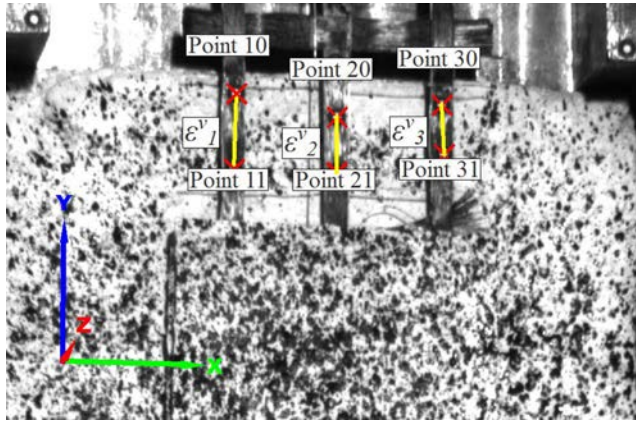
Fig. 3 Definition of virtual strain gages (VSGs), specimen C_28_3
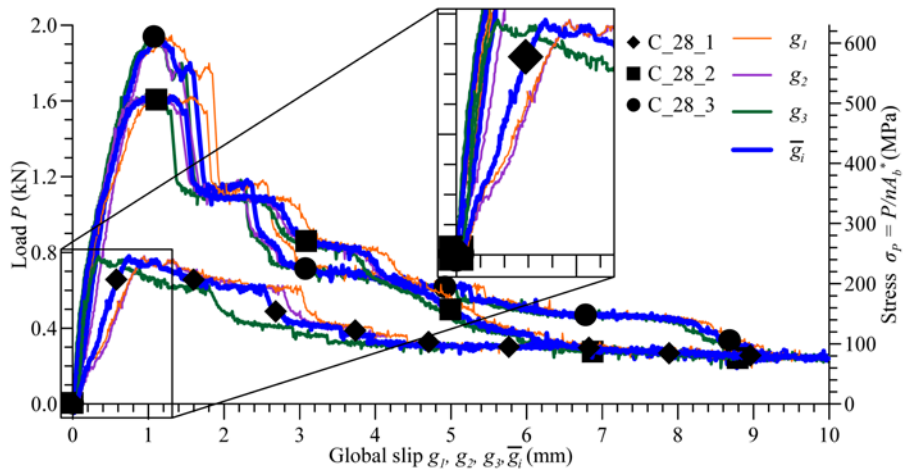
Fig. 4 Applied load P and normal fiber stress σ_P - global slip g response of tested specimens, average global slip $\bar{g}_i$ and individual bundle global slip g_i
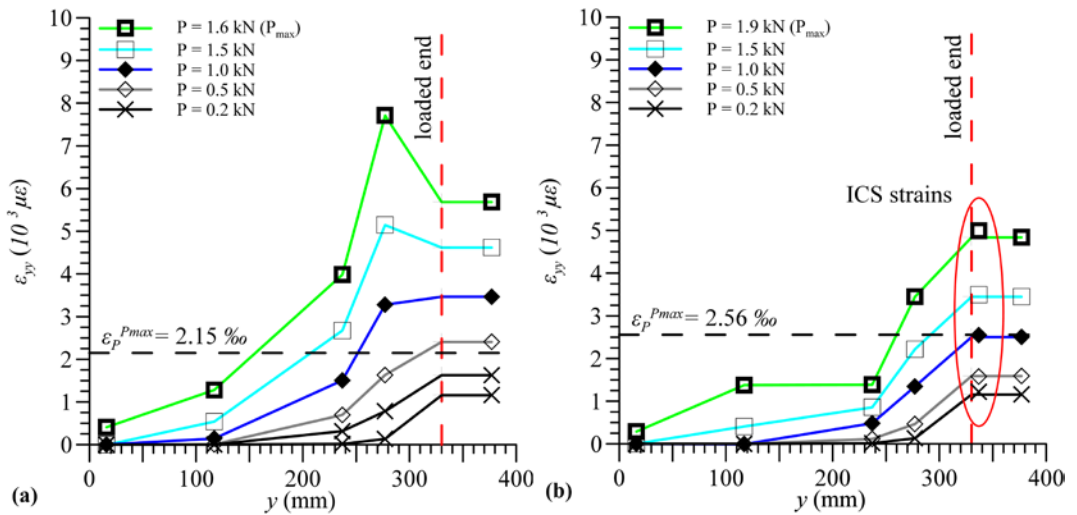

Fig. 5 Strain profiles along length of central longitudinal fiber bundle at different applied load levels for (a) specimen C_28_2 and (b) C_28_3 (measurements circled correspond to values of strain ε_2^v determined by ICS)
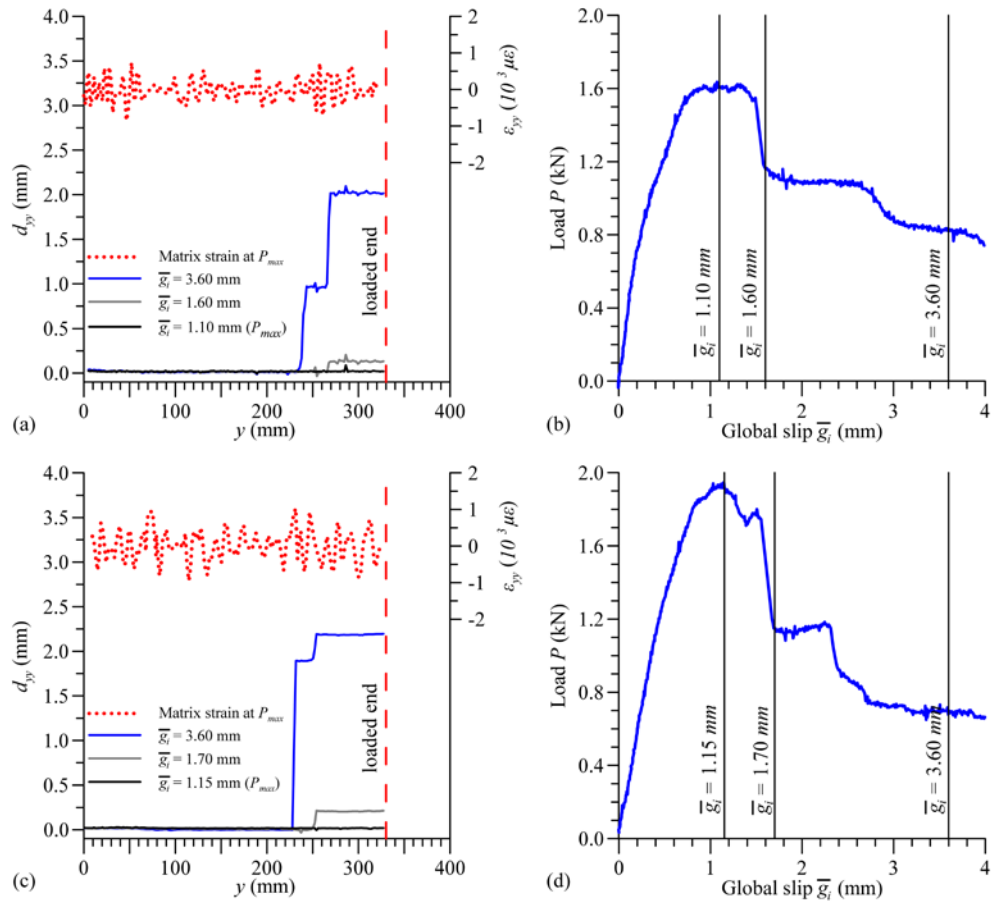
**Fig. 6** Specimen C_28_2 (a) matrix surface longitudinal displacement d_{yy} at x = 7.5 mm and matrix surface longitudinal strain ε_{yy} at maximum load, and (b) corresponding load P - $\overline{g}_i$ response; Specimen C_28_3 (c) matrix surface longitudinal displacement d_{yy} at x = 7.5 mm and matrix surface longitudinal strain ε_{yy} at maximum load, and (d) corresponding load P - $\overline{g}_i$ response
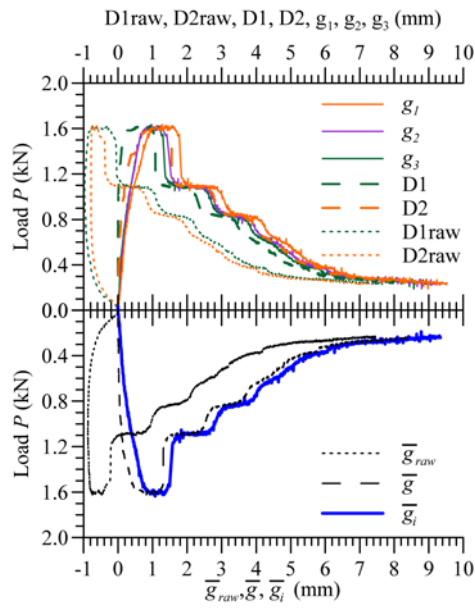
Fig. 7 Load P versus LVDTs displacement and global slip g_i measurements (top) and load P versus $\bar{g}_{raw}$ (average of D1raw and D2raw), $\bar{g}$ (average of D1 and D2), and $\bar{g}_i$ (average of $\bar{g}_1$, $\bar{g}_2$, and $\bar{g}_3$) (bottom) for specimen C_28_2
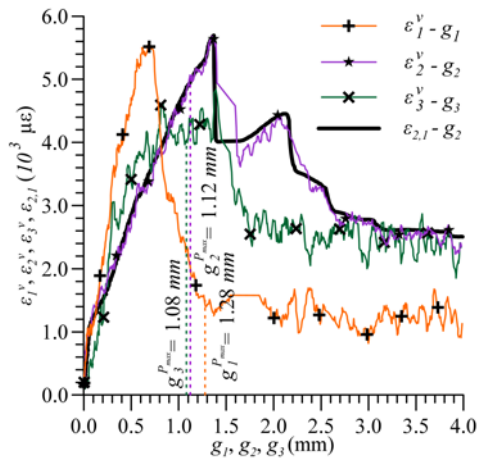

Fig. 8 Strain at loaded end ε_i^v - global slip g_i (for each bundle) for specimen C_28_3 (dashed lines indicate the value of global slip in each bundle at maximum load g_i^{Pmax})